46th AIAA/ASME/ASCE/AHS/ASC Structures, Structural Dynamics & Materials Conference
18 - 21 April 2005, Austin, Texas

AIAA 2005-1884

The ST8 SAILMAST Validation Experiment

Michael E. McEachen*, Thomas A. Trautt† and David M. Murphy‡
ATK Space Systems, Goleta, CA 93117

The SAILMAST Validation Experiment employs an ultra-light graphite Coilable boom in a Scalable Architecture for the Investigation of the Load Managing Attributes of a Slender Truss. The investigation will validate the strength and stiffness attributes of versatile gossamer boom technology through correlation of in-flight measurement with analytical prediction. Successful flight validation of deployable gossamer truss technology is a critical step forward in risk mitigation to make gossamer spacecraft systems a reality, enabling new classes of missions. Propellantless propulsion (solar sailing), large aperture sensors, and applications not yet conceived will be made feasible through the validation of this fundamental building block of gossamer structure. Analysis tools and techniques have been developed, correlated, and scaled to the proposed experiment system in order to predict on-orbit behavior and verify the suitability of measurement range and accuracy to ensure a successful, informative flight validation experiment.

Nomenclature

a	=	longeron eccentricity
C	=	follower load length
e	=	mast eccentricity under load
EI	=	bending stiffness
FEM	=	Finite Element Model
GA	=	shear stiffness
ISP	=	In-Space Propulsion
L	=	mast length
L_{bay}	=	mast bay length
NMC	=	New Millennium Carrier
NMP	=	New Millennium Program
P	=	applied load
P_{cr}	=	critical buckling load
Q	=	shear force
T	=	lanyard load
ULGC	=	Ultra Light Graphite Coilable
y_{tip}	=	tip deflection
θ	=	loading angle
ρ	=	radius of curvature

I. Introduction

GOSSAMER applications pose new challenges in spacecraft architecture consisting in large part of deployable space structure - where mass and stowed volume effectiveness are particularly critical, as these metrics together drive launch costs. Solar sailing[1,2] is the ideal example: very large structures are required, and low mass is crucial since thrust is inversely proportional to the mass needed to deploy and stabilize the reflective sails. The volume of the stowed sail system must not drive the payload to a larger launch vehicle, as this may offset the cost savings of

* Senior Mechanical Engineer, ATK Space Systems, 600 Pine Ave, Goleta, CA 93117, Member AIAA
† Senior Mechanical Engineer, ATK Space Systems, 600 Pine Ave, Goleta, CA 93117
‡ Chief Research Engineer, ATK Space Systems, 600 Pine Ave, Goleta, CA 93117, Member AIAA

this new propulsion technology. Stiffness is not generally a driving requirement, since it has been accepted by the gossamer community that the sailcraft attitude and trajectory control system must be engineered to function with the gossamer structure's modal response is critical to the viability of these structures in real applications.[3] Therefore, a gossamer truss has slender, strength-based, structural elements. As elements are made more slender, they become more susceptible to waviness. This waviness is caused by the manufacture of the composite and by minute inaccuracies in assembly from bay to bay. Additionally, since the truss itself is slender it is also subject to global bow and twist from manufacturing inaccuracy and thermal distortion. In the gossamer regime the potential range of local and global imperfections can combine in complex ways to reduce load-carrying capability.

NASA's New Millennium Program (NMP) recognizes the importance of validating gossamer boom technology within the zero gravity environment provided uniquely by a flight experiment and has funded efforts to develop pertinent technology validation plans. The work described herein was performed under a Concept Definition (study phase) contract. The experiment under development for the eighth NASA NMP Space Technology (ST8) flight program is a **S**calable **A**rchitecture for the **I**nvestigation of the **L**oad **M**anaging **A**ttributes of a **S**lender **T**russ. The SAILMAST experiment plan provides a thorough investigation of the fundamental attributes of an ultra-lightweight (slender) Coilable truss, allowing extrapolation to generalized gossamer truss structures that may be different in geometry, loading, or design. These efforts will reduce the risk to the first users of gossamer structure technologies, allowing incorporation into science missions to occur at an accelerated pace. The SAILMAST experiment will provide validation of the most fundamental building block of gossamer space structure technology and, in particular, the essential element needed for near term solar sailcraft to support key NASA roadmap missions.

For the ST8 Concept Definition Phase, a 7-m length of gossamer SAILMAST structure was built and tested in a 1g (laboratory) environment. This technology stows in less than 1% of its deployed length. The linear mass of this structure is 34 g/m, which is less than 15% of the mass of comparable flight heritage structures and less than 50% of the mass of the sail mast structure built in 2003 under the NASA In-Space Propulsion (ISP) Solar Sail Ground System Demonstrator program.[4,5] Static and dynamic bending tests of this most advanced gossamer structure were performed and correlated with a Finite Element Model (FEM) of the test system as well as a newly developed analytical treatment for slender trusses. This effort has brought the technology readiness level (TRL) to 4. The follow-on activities in the Formulation Refinement and Implementation phases are carefully planned to increase incrementally, with managed risk, the experiment definition with progressively higher-fidelity analysis tools, hardware, and test environments.

II. Technology Validation Experiment Objectives

In order for the flight experiment to be considered a success it must measure the global shape of the mast and obtain the degree of bow, and it also must quantify the load capability of the mast. Measured results must have sufficient fidelity to allow identification of the influence of separate effects, i.e. photogrammetric measurement of global bow must be sufficiently accurate to discern distortions that have an effect on strength within the predictive accuracy of the analysis. By looking at sources of error, and correlation with hardware testing performed during the Study Phase, a reasonable assessment of our analytical predictive accuracy has been achieved. The model correlates with test results within 3%, in the range tested so far. Further insight into the performance of long slender booms will be possible with refinements to the model made after testing and correlation with the full-length test boom, as well as a reduction in predictive error. The scalability of the experiment's results will be established by dual-measurement-method correlation of test results with predicted values. The two data acquisition methods are independent and are configured to capture similar data with a similar level of accuracy.

Parametric studies will be performed on the 40-m boom in order to access validity of the model under a wide range of potential circumstances. In particular, the global bow can be deliberately adjusted by external means, and the stiffness and load capability assessed. This will enable flight data acquisition throughout a range of possible free-state shape conditions. Along with validating the applicability range of the analytical model, the hardware itself will prove out the range of possible global distortion that may be accommodated by the loading and imaging techniques planned for flight.

The performance of the flight structure will, of course, be investigated in the laboratory environment prior to flight. The SAILMAST will be supported to negate, to the extent possible, the effects of gravity on shape. Load versus deflection experiments, analogous to the flight regimen, will be measured and compared with those predicted by the models, accounting for measured global and local shape. In order to provide a range of data points for analytical correlation, known distortions will be induced to the local and global mast shape. Mast displacement will be measured both by the flight video method and by a laser target tracker. While true free-state shape will be impossible to generate in 1g, measuring the shape in two orthogonal positions, then combining the data will

approximate the 3-d shape. This data can then be input to the FEM and the analytical model, and sources of variance diagnosed. By the end of this phase, there will be high confidence in the precision of predictive capability provided by the analytical model.

The planned Formulation Refinement activity includes fabrication of the flight experiment mast, while the Implementation Phase will provide the remainder of the flight hardware involved in the experiment. This will allow system-level testing to be performed, ensuring that the experiment will function as planned and provide the desired measurements, with the range and precision required to achieve the post-flight TRL of 7. The 40-m structure will be integrated with the stowage canister, hold-down release and other structure and mechanisms used for flight, as well as video, telemetry and accelerometers necessary for the in-flight experiment. The complete system will be tested as proto-flight hardware to establish final mass properties, functional deployment capability, stowed sine and random vibration testing, thermal cycling survivability, and deployed stiffness and buckling strength.

III. Validation Flight Experiment Scenario

The in-space experiment will begin by deploying the SAILMAST from the stowage canister, to zenith, by paying out a lanyard with a motor. When the boom is deployed 80%, the spacecraft ACS may be placed on standby, since the mast will provide gravity gradient stabilization, allowing the dynamics of the coilable kick-over to be recorded. Upon full deployment, a baseline measurement of mast shape will be performed by photogrammetric analysis of targets as imaged by a video camera mounted at the mast root. Actuation of piezos in line with the 3 longerons, at their root, will induce small oscillations of the structure as a sine input is swept. The tip accelerometer and videogrammetry will observe the first mode response amplification, and the damping after the input force succession. The mast shape will then be entered into the mast sizing spreadsheet. Next, the motor will be slowly reversed, pulling on the lanyard, until a known axial load has been applied to the boom, measured by a load cell on the lanyard pulley. This load will have produced some displacement in the mast, to be measured by again taking images with the root camera. This process is repeated at several loads until additional lanyard stroke does not increase lanyard load, at which point the mast will be "buckled". The load is then reduced, and images taken as before, at increments until the load has been fully removed.

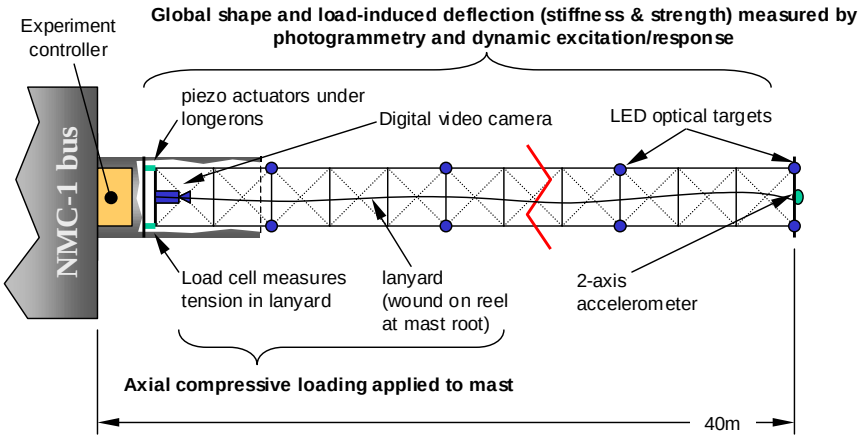

Figure 1. Experiment Functional Diagram

IV. Predictive Models

The majority of effort expended during the Study Phase was devoted to developing and refining analytical models. Without highly accurate, refined models, the flight experiment would only represent a single design data point. However, the modeling performed and correlated with the 7-m mast justifies TRL 4 status, and when the full-length hardware is built and tested, the models' scalability and applicability to truly slender, gossamer hardware will have been validated. In the section below, both finite element and closed-form mathematical modeling is described.

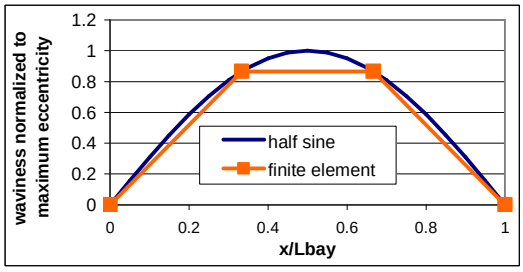

Figure 2. Local Waviness Approximation

A. Modeling Longerons

There are several steps involved in modeling the SAILMAST longerons in the finite element model. The buckling load of a bay length of the longeron with simply

supported ends is computed using a closed from solution and a simple finite element model. The ratio of the two buckling loads is used to adjust the area moments of inertia in the finite element model such that the buckling load in the finite element model matches the theoretical buckling load. This procedure works well to simulate the longeron axial stiffness in pre-buckled and post-buckled configurations. The number of (equal length) elements per bay was set to 3 to minimize computational requirements while still providing realistic modeling of the waviness effect. A correction of the effective area moment of inertia was also made to make the reduced-element bay match a finely meshed (test) version. Confirming that a small number of elements per bay per longeron can simulate local waviness was a critical step. Local waviness is assumed to take the form of a half sine over one bay length. Locating the nodes of the finite element model on the half sine curve as shown in Figure 2 gave excellent results, with the understanding that the eccentricity of the two nodes between the batten frames is 0.866 times the maximum eccentricity to be simulated.

Assuming small angular rotations, the theoretical deflected shape for an axial loaded simply supported column with an initial half sine is[6]

$$y(x) = \frac{y_0(x)}{1 - \frac{P}{P_{cr}}} \tag{1}$$

where

$$y_0(x) = a \cdot \sin\left(\frac{\pi \cdot x}{L_{bay}}\right) \quad \text{and} \quad P_{cr} = \frac{\pi^2 \cdot E \cdot I}{L_{bay}^2} \tag{2), (3)}$$

In these equations, L_{bay} is the length of the column, EI is the bending stiffness parameter, $y_0(x)$ is the initial shape, y(x) is the shape under axial load, P, and P_{cr} is the buckling load. The axial load causes a shortening of the column, ΔL, due to compressive strain and flexure.

$$\Delta L = \frac{P \cdot L_{bay}}{E \cdot A} + \int_0^L \frac{1}{2} \cdot \left(y'_{tot}(x)^2 - y'_0(x)^2 \right) dx = \frac{P \cdot L_{bay}}{E \cdot A} + \left[\frac{1}{\left(1 - \frac{P}{P_{cr}}\right)^2} - 1 \right] \cdot \frac{\pi^2 \cdot a^2}{4 \cdot L_{bay}} \tag{4}$$

In Eq. (4), 'a' is the maximum eccentricity. The load deflection curve from the three-element longeron is compared to the theoretical closed form solution and to a 20-element longeron in Fig. 3. The local eccentricity used in this comparison is 0.254 mm. The three-element longeron has the reduced area moments of inertia and the eccentricity of the two nodes is 0.866 times the eccentricity. All three load-deflection curves match well for strains below 10%. The load difference between the 3-element and the 20-element model is less than 10% for strains up to 50%.

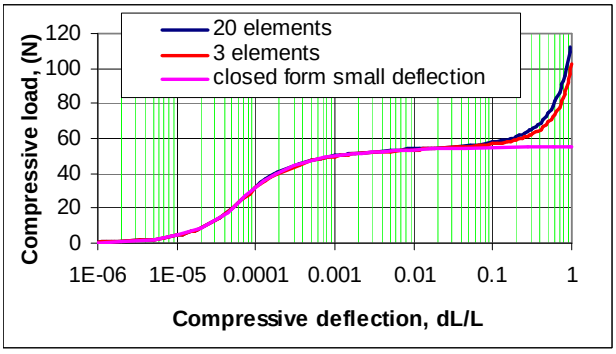

Figure 3. Load Deflection Curves with 0.254 mm Local Eccentricity

B. Finite Element Model of 50 Bay Mast

A 50 bay FE model was created to compare to test results from the 50-bay mast. The bay length and diameter are equal to those of the 7-m mast. The finite element model has three elements per bay per longeron with the properties and derived area moments of inertia of the previous section. In the actual hardware, the battens are buckled in the deployed configuration to provide tensile preloads in the diagonals and compressive preloads in the longerons. In the finite element model, the battens are modeled as link elements that carry only tensile and compressive loads. Thermal strains are applied to the battens to make them expand in the model and produce a batten preload of 6.294 N. The finite element batten stiffness is very low to simulate the almost constant load of the actual buckled battens. The diagonal length specified on the engineering drawing applies under the actual tensile preload. To account for the preload strain, an initial strain is applied to the diagonals in the finite element model. The corner fittings are modeled as point masses. The piezo actuators at the root of each longeron are modeled as link elements, as shown in Fig. 4. The cantilevered beam, which flexes under the action of the piezo, is modeled as a beam element with one end fixed. There are moment releases at the interfaces with the longerons. In the actual hardware, the leaf springs are part of an aluminum root plate. The tip plate is also aluminum and is modeled with beam elements as shown in Fig. 4. There are moment releases at the interfaces with longerons to simulate the end joints. Additional tip mass as added at the ends of the longerons as point masses.

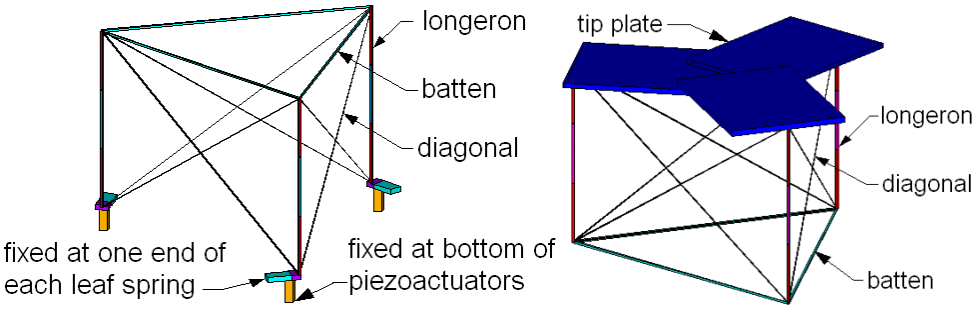

Figure 4. Root Bay and Tip Bay

C. Closed-Form Mast Modeling

In this section, closed form solutions are derived for lateral deflections of the mast as a function of lanyard load. The closed form solution will be compared to the finite element model. Global waviness is included as an initial deflection in the beam-column differential equation. The local waviness is accounted for by iteratively solving for the bending stiffness parameter, EI, which satisfies the beam column differential equation and also matches the effective EI due to reduction in stiffness of the longerons under the applied loads and resulting deflections.

The analysis is similar to work done by Crawford and Benton[7] and others,[8] with several modifications. Shear deflection has been added. The initial global deflected shape has been changed from a quarter sine to a quadratic shape to simulate a constant curvature. The global bow direction has been changed from the general case to the worst-case direction for buckling strength that was shown in the previous work to be toward a longeron. The mast loading direction has been changed from a root-fixed lanyard (as in the experiment) to the general case where the load effectively pulls from behind the root as in a solar sail. The EI has been changed from the more conservative tangent EI to an effective EI. The effective EI is the moment over the curvature and is more accurate for computing total curvature under static loading. The tangent EI is the rate of change of moment over the rate of change of curvature and is more accurate for computing natural frequencies and vibrations about some deformed shape.

1. Solution to Beam-Column Differential Equation

The closed form solution is derived for the loading configuration shown in Fig. 5

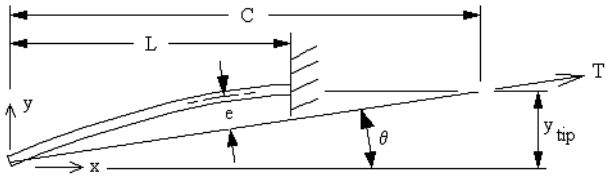

Figure 5. Mast with Applied Lanyard Load

The initial shape of the beam prior to applying any lanyard load is assumed to be quadratic in x as follows:

$$y_0(x) = b\cdot\left[1-\left[\left(\frac{L-x}{L}\right)^2\right]\right] \tag{5}$$

In Eq. (5), b is the initial deflection at the tip. The curvature due to bending moments is given by the following equation where M is the bending moment with the sign convention shown in Fig. 6, $y_b(x)$ is the bending deflection and the primes indicate derivatives with respect to x.

$$y''_b(x) = \frac{M}{EI} = \frac{-T\cdot\cos(\theta)\cdot y(x) + T\cdot\sin(\theta)\cdot x}{EI} \tag{6}$$

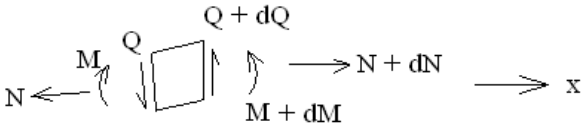

Figure 6. Differential Element Showing Sign Convention for Moment and Shear

The shear force, Q, in the mast is approximated by the following equation where y(x) is the total displacement including initial displacement and displacements due to applied loads.

$$Q(x) = T\cdot\sin(\arctan(y'(x)) - \theta) \approx T\cdot(\arctan(y'(x)) - \theta) \approx T(y'(x) - \tan(\theta)) \tag{7}$$

Slope due to shear is given by the following equation where GA is the shear stiffness parameter of the mast.

$$y'_s(x) = \frac{Q(x)}{GA} = \frac{T\cdot(y'(x) - \tan(\theta))}{GA} \tag{8}$$

The total curvature due to bending, shear and initial shape is

$$y''(x) = y''_b(x) + y''_s(x) + y''_0(x) \tag{9}$$

Equations (5), (6), (8) and (9) are combined to obtain the beam-column differential equation.

$$y''(x) + \frac{T\cdot\cos(\theta)\cdot y(x)}{EI\cdot\left(1-\frac{T}{GA}\right)} = \frac{T\cdot\sin(\theta)\cdot x}{EI\cdot\left(1-\frac{T}{GA}\right)} + \frac{-2\cdot b}{L^2\cdot\left(1-\frac{T}{GA}\right)} \tag{10}$$

The general solution to this equation is of the following form where C_2, C_3, and θ are dependent on the boundary conditions.

$$y(x) = -C_1 + C_2\cdot\sin(\lambda\cdot x) + C_3\cdot\cos(\lambda\cdot x) + x\cdot\tan(\theta) \tag{11}$$

where

$$\lambda^2 = \frac{GA \cdot T \cdot \cos(\theta)}{EI \cdot (GA - T)} \quad \text{and} \quad C_1 = \frac{2 \cdot b \cdot GA}{\lambda^2 \cdot L^2 \cdot (GA - T)} \tag{12) \& (13)}$$

The constants C_2, C_3, and θ are dependent on the following boundary conditions.

$$y(0) = 0 \qquad y(L) = y_{tip} \qquad \tan(\theta) = \frac{y_{tip}}{C}$$

$$y'(L) = y'_s(L) = \frac{T \cdot (y'(L) - \tan(\theta))}{GA} \quad ==> \quad y'(L) = \frac{-y_{tip}}{C} \cdot \frac{T}{GA - T} \tag{14}$$

Applying the boundary conditions leads to the following results where L/C can be set to zero for the case where C is infinite.

$$y(x) = C_1 \cdot (\cos(\lambda \cdot x) - 1) + C_2 \cdot \sin(\lambda \cdot x) + \frac{y_{tip}}{L} \cdot \frac{L}{C} \cdot x \tag{15}$$

$$y_{tip} = C_1 \cdot \left[\frac{\lambda \cdot L \cdot (1 - \cos(\lambda \cdot L))}{\frac{L}{C} \cdot \left(\frac{GA}{GA - T} \right) \cdot \sin(\lambda \cdot L) + \left(1 - \frac{L}{C} \right) \cdot \lambda \cdot L \cdot \cos(\lambda \cdot L)} \right] \tag{16}$$

$$C_2 = C_1 \cdot \sin(\lambda \cdot L) + \left[\left(1 - \frac{L}{C} \right) \cdot \sin(\lambda \cdot L) - \frac{L}{C} \cdot \left(\frac{GA}{GA - T} \right) \cdot \frac{\cos(\lambda \cdot L)}{\lambda \cdot L} \right] \cdot y_{tip} \tag{17}$$

The EI that satisfies the differential equation for an assumed load and λ is derived from Eq. (12):

$$EI = \frac{GA \cdot T}{\lambda^2 \cdot (GA - T)} \cdot \left[\sqrt{1 + \left(\frac{y_{tip}}{L} \cdot \frac{L}{C} \right)^2} \right]^{-1} \tag{18}$$

For any chosen fixed value of λ, T can be varied until EI from Eq. (18) matches the effective EI due to the loading, derived in the following section.

2. Effective Mast EI as a Function of Longeron Initial Eccentricity and Axial Load

The bending moment in the mast is given by Eq. (6). The moment equation is combined with the boundary condition, $\tan(\theta) = y_{tip}/C$, and some trigonometric identities to obtain the following equation.

$$M(x) = T \cdot \left(-y(x) + \frac{y_{tip}}{L} \cdot \frac{L}{C} \cdot x \right) \cdot \left[\sqrt{1 + \left(\frac{y_{tip}}{L} \cdot \frac{L}{C} \right)^2} \right]^{-1} \tag{19}$$

The maximum moment occurs when the derivative is zero.

$$0 = -y'(x) + \frac{y_{tip}}{C} \tag{20}$$

The location of the maximum moment is derived by combining Eq. (20) with Eq. (15).

$$x_0 = \frac{1}{\lambda} \cdot \operatorname{atan}\left(\frac{C_2}{C_1}\right) \tag{21}$$

The maximum eccentricity also occurs at x_0 and is given by the following equation.

$$e = \frac{-M(x_0)}{T} = \left(y(x_0) - \frac{y_{tip}}{L} \cdot \frac{L}{C} \cdot x_0\right) \cdot \left[\sqrt{1 + \left(\frac{y_{tip}}{L} \cdot \frac{L}{C}\right)^2}\right]^{-1} \tag{22}$$

The loads on the longerons except for the diagonal preloads are shown in Fig. 7. The compressive loads in the longerons are as follows where P_0 is the preload due the diagonals.

$$P_1 = P_0 + \frac{T}{3} - \frac{2}{3} \cdot \frac{M}{R} \quad \text{and} \quad P_2 = P_0 + \frac{T}{3} + \frac{1}{3} \frac{M}{R} \tag{23),(24}$$

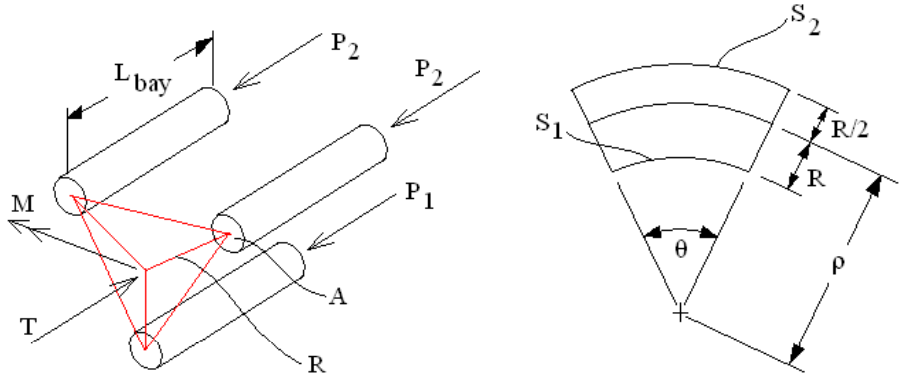

Figure 7. Loads on Longerons and Mast Radius of Curvature

The local buckling load for the longeron is given by the following equation, where E is the Young's modulus of the longeron and I is the area moment of inertia of one longeron.

$$P_{cr} = \frac{\pi^2 \cdot E \cdot I}{L_{bay}^2} \tag{25}$$

The local waviness is assumed to be a half sine shape over one bay length of the longeron with amplitude, 'a'. The effective tensile strain including the shortening of the longeron due to bending is as follows where P is the compressive load in the longeron and A is the cross section area of the longeron. This equation is derived from Eq. (4).

$$\varepsilon_1 = -\left[\frac{P_1}{E\cdot A} + \left[\left(\frac{P_{cr}}{P_{cr} - P_1}\right)^2 - 1\right]\cdot\left(\frac{\pi\cdot a}{2\cdot L_{bay}}\right)^2\right] \tag{26}$$

Although the neutral axis shifts, the global displacements and loads are at the zero-load neutral axis. The radius of curvature of the zero-load neutral axis is derived below with the aid of Fig. 7. The arc lengths of the outer fibers are

$$S_1 = (\rho - R)\cdot\theta = (1 + \varepsilon_1)\cdot S_0 \quad \text{and} \quad S_2 = \left(\rho + \frac{R}{2}\right)\cdot\theta = (1 + \varepsilon_2)\cdot S_0 \tag{27),(28}$$

These equations are combined to derive the radius of curvature, ρ.

$$\rho = R\cdot\frac{(3 + 2\cdot\varepsilon_2 + \varepsilon_1)}{2\cdot(\varepsilon_2 - \varepsilon_1)} \tag{29}$$

The effective EI is

$$EI_{eff} = -M\cdot\rho = -M\cdot R\cdot\frac{(3 + 2\cdot\varepsilon_2 + \varepsilon_1)}{2\cdot(\varepsilon_2 - \varepsilon_1)} \tag{30}$$

When $\varepsilon_1 = \varepsilon_2$, this equation blows up. This can be prevented by replacing M with Eq. (31).

$$M = (P_2 - P_1)\cdot R \tag{31}$$

Equations (26), (30) and (31) are combined to obtain the following equation.

$$EI_{eff} = EI_0\cdot\frac{\left(1 + \frac{2\cdot\varepsilon_2}{3} + \frac{\varepsilon_1}{3}\right)\cdot(P_{cr} - P_1)^2}{\left[(P_{cr} - P_1)^2 + \frac{P_{cr}^2\cdot(2\cdot P_{cr} - P_1 - P_2)}{(P_{cr} - P_2)^2}\cdot\left(\frac{\pi\cdot a}{2\cdot L_{bay}}\right)^2\cdot E\cdot A\right]} \tag{32}$$

where

$$EI_0 = \frac{3}{2}\cdot R^2\cdot E\cdot A \tag{33}$$

In this equation, EI_0 is the stiffness of a straight mast without local waviness. Other useful loads are the shear loads at the root and tip which are derived from equations (7), (14) and (15).

$$Q_{root} = Q(L) = -T\cdot\frac{y_{tip}}{L}\cdot\frac{L}{C}\cdot\left(\frac{GA}{GA - T}\right) \tag{34}$$

$$Q_{tip} = Q(0) = T \cdot C_2 \cdot \lambda \tag{35}$$

3. Iterative Solver

The key to making use of the closed-form equations derived above is by their incorporation into an iterative solver. With this tool, for any given λ a range of T is automatically generated, and successively refined to narrow the difference between EI that satisfies the differential equation and the effective EI that accounts for mast loading. Fig. 8 illustrates a portion of this spreadsheet, showing the values of T converging closer with each iteration.

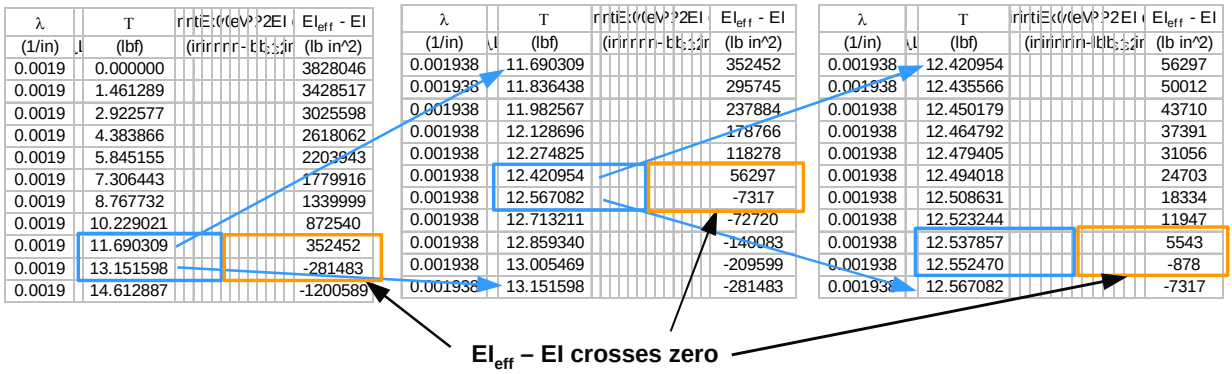

Figure 8. Iteratively Finding T for Given λ

4. Closed Form and Finite Element Comparison

The parameters of the 50 bay mast were programmed into the solver described above to compute compressive load versus deflection curves. The results for the 50 bay mast with L/C =0 and two different initial waviness configurations are compared to finite element results in Fig. 9. Gravity is not included in the models. In both cases, the closed form buckling strength is about 7% less than the finite element results. In the closed form solution, the effective EI at the maximum moment location is applied to the whole length of the mast and therefore results in a lower strength than the finite element model. Another important effect may be due to the fact that the closed form solutions do not yet account for the post-buckled stiffening effect. This effect will be included in future analysis efforts.

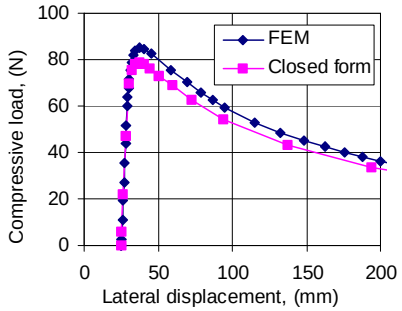

Figure 9. Closed Form Load-Deflection Compared to Finite Element, 25.4 mm Initial Tip Offset, 0.0676 mm Local Eccentricity

The post-buckled shape from the finite element model is shown in Figure 10. Figure 11 illustrates the very close agreement in the deflected shape between the FEM and closed-form methods. The difference in load between the two methods is due to the more conservative assumptions for EI used by the closed-form model.

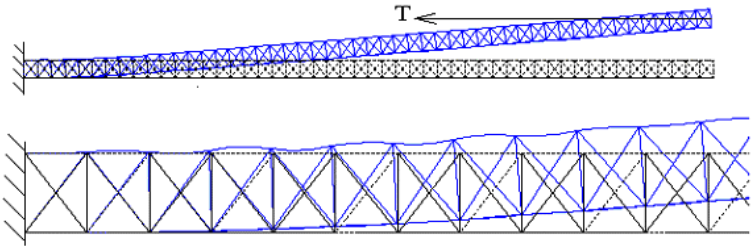

Figure 10. Buckled Mast

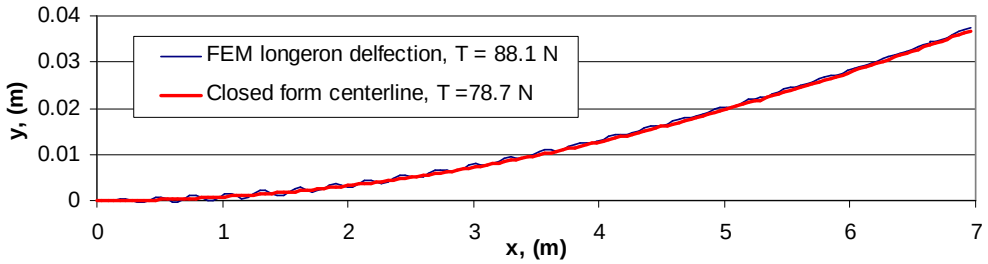

Figure 11. Closed Form Deflected Shape Compared to FEM at Max Load, 0.025 m Initial Tip Offset, 0.076 mm Initial Local Offset

V. In-Flight Experiment Operation

In conjunction with the boom technology, there are a number of unique elements required to execute the SAILMAST flight experiment, particularly related to the challenge of operating the experiment remotely. Remote testing requires the use of specialized actuators and sensors that must operate effectively in the particular regime applicable to our experiment. The standard methods used for ground-based structural characterization are not practical, and the realities of the flight experiment environment must be accounted for in the analytical modeling.

The planned in-flight test configuration has been designed to accommodate a wide range of initial global bow and capture the maximum load capability as illustrated in Fig. 12, below. The deflection at maximum load for all foreseeable initial conditions falls within the limits of measurable deflection.

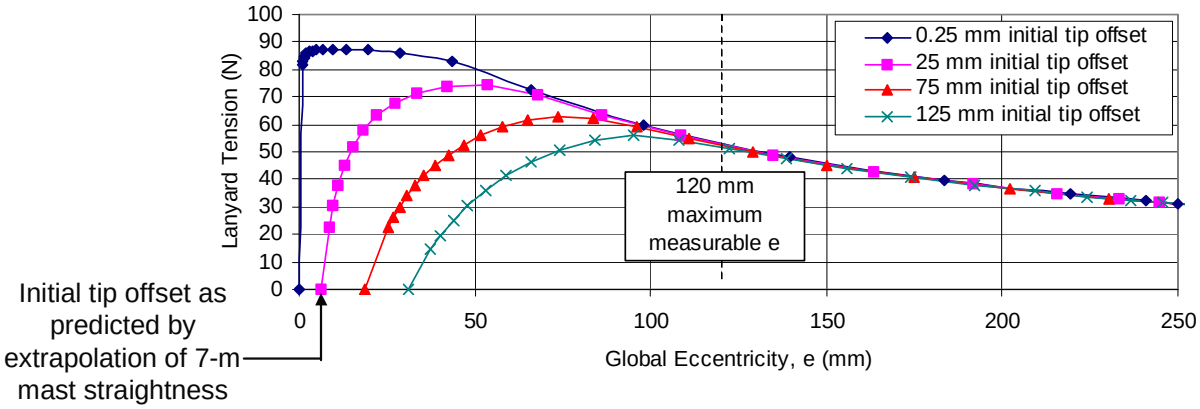

Figure 12. Global Eccentricity vs. Load, 0.025 mm Longeron Local Eccentricity

A. Videogrammetry

The deployed free-state shape of the gossamer structure is has a significant effect on its axial load carrying capability, and this relation is a fundamental investigation of the SAILMAST experiment. A simple yet robust method for measuring this shape is provided by photogrammetry. Targets placed at discrete stations along the length of the (zenith-pointed) mast are visible as distinctly bright spots in an otherwise dark image, and the location of those spots will be analyzed to determine the straightness of the boom.

The SAILMAST experiment will utilize a version of a flight-proven video system[9]. The video system consists of a camera, lens, and controller unit. The requirements for this system are driven by the conditions of the proposed experiment, and relate to the capability of

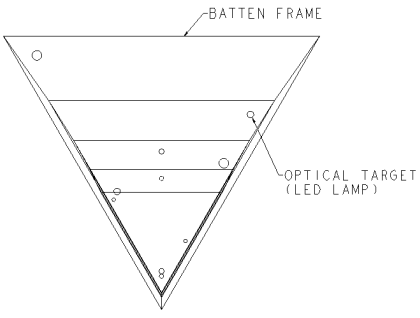

Figure 13: Simulated View Down Bent Mast

resolving distortions in the boom that affect its stiffness. A spreadsheet has been developed to calculate these requirements, based on camera pixel density, optical clarity, depth of field, and target distance.

The in-flight photogrammetry takes advantage of the perspective view available along the mast centerline. This allows targets to be placed similarly on batten stations distributed along the length without obstructing the camera view of outboard targets. Figure 13 shows a computer-generated perspective view down the mast from the root. This view illustrates a mast bowed by 7 cm at the tip, exceeding the expected worst-case bow in the actual mast. More severe bend may still be measured, but without the ability to accurately gauge twist since only a single target of the outermost stations will be visible. As may be seen, all the targets are still visible from the root, and therefore may be used to indicate the relative straightness of the boom.

The assumption for photo-based measurements is usually that a super-high resolution image is required to provide sufficient accuracy for meaningful data. This results in very high hardware development cost, as well as burdensome data rates. The SAILMAST experiment benefits from the fact that the targets to be tracked are very close together, so the field of view of the imager can focus on a narrow field of view. This optimizes the amount of data captured by the available pixels, and means that a standard space flight imaging sensor will provide sufficient definition to resolve boom distortions of the magnitude significant to strength performance. For example, the standard video-imaging sensor with a 75 mm focal length lens, on a 40-m boom can resolve 2.2 mm of tip displacement, which translates to a 2% uncertainty on load capacity. Assessing these requirements has indicated that the imaging specifications are neither too stringent, resulting in high development cost and risk, nor too relaxed to provide adequate measurement of global shape. Figure 14 is a digital photograph taken directly from a mockup of the boom geometry, using the same pixel density as the standard camera sensor. No image enhancement (i.e. contrast or sharpening) has been performed, only a negative transform for document printing purposes.

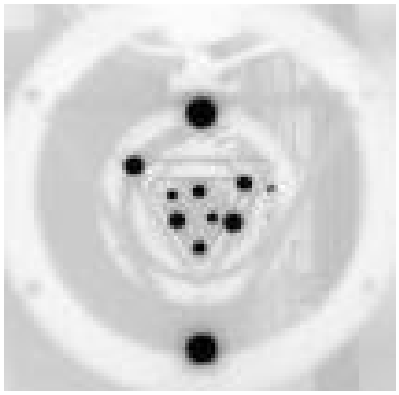

Figure 14: Camera View Down Mast

Once the video data files are downloaded, the mast deflection and dynamics are interpreted using optical target tracking software. This software calculates X- and Y- target positions frame by frame, with the Z- axis (along the mast length) positions pre-programmed, and used to scale the motion of the targets. This data will be compared with predicted performance and any discrepancies will be diagnosed.

B. Piezoelectric Actuators & Controller

Actuators are used to dynamically excite the SAILMAST so that the stiffness may be understood as a function of axial load. Piezos are mounted in line with each longeron at the root of the boom. Special features at the mast root are required to allow the piezo actuators to function efficiently. The objective is to allow the linear displacement of the piezo stack, which is on the order of 30 µm (0.0007 in.), to act directly on the longeron. The actuators' motion is transferred from the piezo to the longerons by a flexible portion in the mast base plate, to which the longeron and moving end of the piezo are attached. The fixed piezo end is grounded to the rigid portion of the base plate, resulting in a structural interface with the stowage canister identical to a non-actuated mast. This technique has been successfully demonstrated on the ISP 20-m S^4 Ground Demonstration System[10] and on the 7-m demonstration mast as shown in Fig. 15. Even on the relatively short 7-m study phase boom, the actuators provided more than enough dynamic displacements to be measured by the consumer-grade digital video camera used. The 40-m flight boom will have increased response as verified by the FEM described earlier.

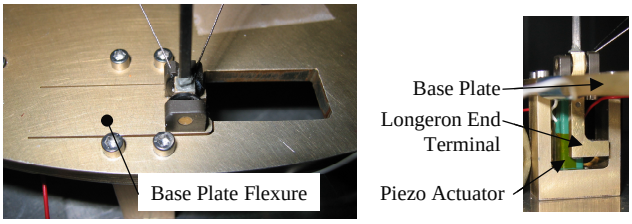

Figure 15. Mast Root Actuator

C. Mast Tip Bridle

In order to demonstrate functional and structural repeatability, three successive deployment and retraction cycles will be performed on the boom. The final retraction is performed after the flight experiment activity has been completed, to allow the spacecraft to resume full 3-axis ACS operation. A tip bridle mechanism is utilized to enable repeated deploy/retract cycles. Though the majority of Coilable boom applications do not require retraction, this feature has been incorporated into previous flight masts. The principle of tip bridle operation is simple: the tension

in the deployment lanyard converted into a torque on the tip relative to the mast longerons, initiating the characteristic helical stowage process. A feature unique to the SAILMAST is that the tip bridle can be locked out, allowing axial loads to be applied to the mast without initiating stowage.

VI. Conclusion

In the Concept Definition Phase of the ST8 SAILMAST program, analysis tools and techniques have been developed, correlated, and scaled to a proposed flight experiment system in order to predict on-orbit behavior, refine a notional design configuration, and verify the suitability of measurement range and accuracy to ensure a successful, informative flight experiment. The flight objectives focus on the measurement of free shape of gossamer Coilable truss technology to correlate and validate models of the effect of global shape on stiffness and strength. Successful flight validation is essential for risk mitigation prior to more detailed formulation of gossamer spacecraft systems that enable new classes of missions, such as propellantless propulsion (solar sailing), large aperture sensors, and other applications yet to be conceived. The models developed and validated by the SAILMAST effort will be invaluable in the design and analysis of future optimized gossamer systems, whatever their scale.

Acknowledgments

The authors wish to recognize Toshio Fujita and John (Jack) Stocky of NASA-NMP (at JPL) for their valuable technical and programmatic support in this effort. The work described herein was performed as part of NMP ST8 Concept Definition Phase contract 1256619 through JPL.

References

[1] Mclnnes, C. R., *Solar Sailing: Technology, Dynamics and Mission Applications*, 1st ed, Springer-Praxis. London, 1999.

[2] Murphy, D., Murphey, T., and Gierow, P., "Scalable Solar-Sail Subsystem Design Concept," *AIAA Journal of Spacecraft and Rockets*, Vol. 40, No. 4, pp. 539-547, July-August 2003.

[3] Murphy, D., and Wie, B., "Robust Thrust Control Authority for a Scalable Sailcraft," *14th AAS/AIAA Space Flight Mechanics Meeting*, AIAA, Washington DC, 2004.

[4] Murphy, D., Trautt, T., McEachen, M., Messner, D., Laue, G., and Gierow, P., "Progress and Plans for System Demonstration of a Scalable Square Solar Sail," AAS 04-105, *14th AAS/AIAA Space Flight Mechanics Meeting*, AIAA, Washington DC, 2004.

[5] Murphy, D., Macy, B., and Gaspar, J., "Demonstration of a 10-m Solar Sail System," 45th *AIAA Structures, Structural Dynamics, & Materials Conference, 5th Gossamer Spacecraft Forum*, Palm Springs, CA, April 19-22, 2004.

[6] Timoshenko, S., *Theory of Elastic Stability*, McGraw-Hill, New York, 1936, pp. 31-33.

[7] Crawford, R.F. And Hedgepeth, J.M., "Effects of Initial Waviness on the Strength and Design of Built-up Structures," *AIAA Journal*, Vol. 13, No. 5, May 1975.

[8] Anderson, M. S., "Buckling of Imperfect Periodic Lattice Structures," *Proceedings of the Symposium, London, England*,., Cambridge University Press, Cambridge and New York, 1983, p. 209-219.

[9] Ridenoure, R.., "RocketCam™ Systems for Providing Space Situational Awareness on Rockets, Spacecraft and Other Remote Platforms," *SPIE Defense & Security Conference*, Proceedings of SPIE Vol. 5418, 2004, pp.94-103.

[10] Murphy, D., McEachen, M., Macy, B., and Gaspar, J., "Demonstration of a 20-m Solar Sail System," *46th AIAA Structures, Structural Dynamics, & Materials Conference, 6th Gossamer Spacecraft Forum*, AIAA, Washington DC, 2005.